

CrossMark
click for updatesCite this: *RSC Adv.*, 2015, 5, 80196

Effect of preparation of Fe–Zr–K catalyst on the product distribution of CO₂ hydrogenation

Xiaojuan Su, Jianli Zhang,* Subing Fan, Qingxiang Ma and Tian-Sheng Zhao*

The precursors of Fe–Zr–K catalysts were prepared by microwave assisted homogeneous precipitation followed by incipient wetness impregnation. The obtained mesoporous particles were small and uniformly shaped. After reduction, the catalyst showed high activity for the selective production of light olefins from CO₂ hydrogenation, superior to the catalyst obtained by co-precipitation. Characterization indicated that with Zr addition, the reducibility, surface basicity and surface atomic composition of the samples varied with the Zr content. The CO₂ adsorption ability of the samples was increased and the samples became hard to reduce as a result of the interaction between iron species and zirconia. In the case of using 5Fe–1Zr–K under selected conditions of 1000 h^{−1}, 320 °C and 2 MPa, the CO₂ conversion and the selectivity of C₂–C₄ olefins reached 54.36% and 53.63%. The olefin/paraffin ratio in the C₂–C₄ hydrocarbon product fraction reached 6.44. The selectivity of CO and C₅⁺ hydrocarbons were 3% and 19.78%, respectively. The catalytic activity remained stable up to 92 h in time-on-stream reaction.

Received 28th June 2015

Accepted 7th September 2015

DOI: 10.1039/c5ra12504a

www.rsc.org/advances

1. Introduction

The increase in CO₂ emissions with industrialization, and the resulting greenhouse effect have given rise to ever-increasing concerns about the disposal of CO₂. The chemical transformation of CO₂ into other chemicals as an avenue for carbon recycling has attracted durative interest.^{1–6}

Compared with the H₂/CO₂–methanol-to-olefins process, direct synthesis of light olefins from CO₂ hydrogenation avoids the methanol synthesis and is more cost-effective. Research suggests that CO₂ hydrogenation to light olefins proceeds in two steps: reduction of CO₂ to CO *via* the reverse water–gas shift (RWGS) reaction, followed by CO hydrogenation *via* the Fisher–Tropsch (F–T) reaction^{7,8} as follows:



Various iron-based catalysts have been studied for this direct process^{9–21} because they are usually adopted in the industrial shift reaction as well as the F–T reaction.²² The catalysts' formulation and preparation procedures obviously affect their performance. Unpromoted iron-based catalysts exhibit high methane selectivity;^{9,10,19} however, the introduction of a potassium promoter results in the enhancement of the carburization of the iron species, formation of iron carbide active phases⁹ and

selectivity of light olefins.^{15,19,20} Several structural supports and chemical promoters have been employed to improve the catalytic performance and to tailor the product distribution.^{11–18} Manganese stabilizes the Fe–K catalyst due to a higher resistance to bulk oxidation, but does not change the product distribution.¹¹ Alumina supported Fe–K shows high conversion of CO₂ and low selectivity of CO and methane at reaction temperature of 400 °C with the C₅⁺ selectivity above 33%.¹² γ-Al₂O₃ supported Fe–Mn–K lowers the formation of methane and increases the product ratio of olefin/paraffin.¹⁷ Zirconia supported K–Fe also displays higher selectivity of light olefins, whereas the CO selectivity was 15%.²³ Up to the present time, the selectivity of CO or methane or both in CO₂ hydrogenation still remains higher. Thus, further reduction of these two side products is desired.

Based on the two-step reaction mechanism of CO₂ hydrogenation to light olefins, the formation of CO or methane may be reduced by tuning the rates of the two reactions. The F–T rate and the WGS rate were shown to be altered with water addition during the F–T synthesis reaction.²⁴ A bifunctional catalyst of ceria modified Fe/Mn/K for olefin production from CO₂ hydrogenation was reported with combining the RWGS and F–T chain growth activity.¹⁸ Zirconia alone provides adsorption sites for the surface reaction intermediates, and the catalytic behavior of metal/zirconia for CO₂ hydrogenation is dependent on metal type and influenced by the interfacial contact area between the metal and zirconia.²⁵ Methane formation is suppressed by H₂O in the WGS reaction over Rh/Fe₂O₃/ZrO₂.²⁶ On the other hand, iron-based catalysts with higher surface areas from micro-emulsion technology exhibit higher activity for CO₂ hydrogenation,¹⁴ and mesoporous xFeMnO by the sol–gel process

State Key Laboratory Cultivation Base of Natural Gas Conversion, College of Chemistry and Chemical Engineering, Ningxia University, Yinchuan 750021, People's Republic of China. E-mail: zhaots@nxu.edu.cn; zhangjl@nxu.edu.cn

enhances CO₂ hydrogenation to C₂–C₅ hydrocarbons.²¹ With a faster reaction rate than the conventional heating, microwave assisted-homogeneous precipitation has shown potential in obtaining catalytic materials with desirable properties such as fine particles and good chemical homogeneity.^{27,28}

In this study, to further understand the role of Zr promoters in iron catalysts for CO₂ hydrogenation to light olefins, Fe–Zr–K catalysts were prepared using microwave assisted-homogeneous precipitation followed by incipient wetness impregnation methods. The effects of the added amounts of Zr on the structural properties of the precursors of Fe–Zr–K catalysts and on the activity for CO₂ hydrogenation were investigated by means of physico-chemical characterization. The influencing mechanism of zirconia on iron catalysts in product selectivity and activity stability was correlated.

2. Experimental

2.1 Sample preparation

The Fe–Zr sample was prepared by the microwave-assisted homogeneous precipitation (MAHP) method with urea as the precipitator. The molar ratios of Fe/Zr included 7 : 1, 5 : 1, 3 : 1 and 1 : 1. The molar ratio of (Fe + Zr)/urea was 1 : 6. In the typical procedure, desired amounts of Fe(NO₃)₃·9H₂O, ZrO(NO₃)₂·2H₂O and urea were mixed in 200 mL of deionized water under stirring until complete dissolution. The solution was then transferred into a Teflon-lined sample holder and reacted under microwave conditions (2450 MHz, 500 W, 1.6 MPa, 170–180 °C) for 2 h. The product was separated *via* centrifugation, washed, and dried at 120 °C overnight and calcined at 500 °C in air for 3 h. The sample without Zr addition was prepared using the same procedure. For comparison, Fe–Zr samples were also prepared by co-precipitation with NH₃·H₂O as the precipitator and marked with suffix [C].

The Fe–Zr–K sample was prepared by incipient wetness impregnation in a fixed Fe/K molar ratio of 10 : 1. The aqueous solution with the desired amount of K₂CO₃ was impregnated on the Fe–Zr sample, and then dried at 120 °C overnight. The obtained samples were named as 7Fe–1Zr–K, 5Fe–1Zr–K, 3Fe–1Zr–K, 1Fe–1Zr–K, Fe–K and 5Fe–1Zr–K[C].

2.2 Sample characterization

X-ray powder diffraction (XRD) patterns were recorded on a Rigaku D/MAX 2200PCX diffractometer with Ni-filtered Cu K α radiation at 40 kV and 30 mA at scanning speed of 8° min^{−1}.

Scanning electron microscopy (SEM) images were obtained on a JEOL-JSM-7500F microscope at 1 kV.

N₂ physical adsorption-desorption isotherms were measured at −196 °C on a JW-BK132F instrument after each sample was pretreated under vacuum at 300 °C for 2 h. The BET surface area was calculated from the adsorption branch. The mesopore and micropore parameter calculation was based on the BJH and HK models, respectively.

H₂ temperature-programmed reduction (H₂-TPR) measurements were carried out on a chemisorption analyzer (TP5000). In a typical procedure, a sample (20–40 mesh) of 70 mg was

pretreated in a quartz tube at 350 °C in He (25 mL min^{−1}) for 1 h and cooled to room temperature. Then, the sample was reduced by a mixed gas composed of 5% H₂ and 95% N₂ as the temperature increased from room temperature to 800 °C at a heating rate of 10 °C min^{−1}. The H₂ consumption was synchronously detected on a gas chromatograph with a thermal conductivity detector.

CO₂ temperature-programmed desorption (CO₂-TPD) was performed on the same TP5000. A 200 mg sample was pretreated at 400 °C for 3 h in a flow of 30% H₂ and 70% N₂ (30 mL min^{−1}), and purged by He (25 mL min^{−1}) for 1 h. CO₂ was then pulse-adsorbed on the sample at 50 °C until saturation, followed by He purge for 1 h. Finally, the sample was heated in He (25 mL min^{−1}) from room temperature to 800 °C at a heating rate of 10 °C min^{−1}. The CO₂ desorption amount was synchronously detected.

X-ray photoelectron spectra (XPS) were obtained on a Thermo SCIENTIFIC ESCALAB 250 equipped with an Al K α X-ray source ($h\nu = 1486.8$ eV) at 15 kV and 10 mA. The background vacuum of the analysis chamber was 2×10^{-9} mbar. The binding energies (BE) were calibrated using the C1s peak at 284.8 eV from adventitious carbon.

2.3 Catalytic activity evaluation

Activity tests were carried out in a flow type fixed-bed system with a stainless steel reactor (350 mm length \times 8 mm i.d. \times 12 mm o.d.). Typical conditions were as follows: precursor packing amount = 2 mL (20–40 mesh), H₂/CO₂ (molar ratio) = 3/1, GHSV = 1000 h^{−1}, $T = 320$ °C and $P = 2.0$ MPa. The sample was first reduced at 400 °C for 8 h by 30% H₂ in N₂ (GHSV = 1000 h^{−1} and $P = 0.1$ MPa). The feed gas was then switched on; the reaction started and proceeded for 96 h of time-on-stream (TOS). The sampling interval was 12 h. The data in Table 3 were obtained at TOS = 68 h. Effluent gas was analyzed on an on-line gas chromatograph (GC-9160) with a $\phi 3$ mm \times 2 m TDX-01 packed column for C₁ product analysis on TCD, and a 50 m \times 0.53 mm \times 40 μ m Al₂O₃ capillary column for C₁–C₅ hydrocarbon product analysis on FID, respectively. Collected liquid products were analyzed on an off-line GC-9160 with a $\phi 3$ mm \times 2 m Porapak Q packed column for aqueous phase product analysis on TCD and a 50 m \times 0.32 mm \times 1.0 μ m HJ-1 capillary column for oil phase product analysis on FID. The data after 48 h time-on-stream reaction were used for the activity discussion. The conversion of CO₂ and the selectivity of products were calculated based on carbon balance.

$$\text{CO}_2 \text{ conv.} = (F_{\text{in}} \times y_{\text{in}}^{\text{CO}_2} - F_{\text{out}} \times y_{\text{out}}^{\text{CO}_2}) / (F_{\text{in}} \times y_{\text{in}}^{\text{CO}_2}) \times 100\%$$

$$\text{CH}_4(\text{CO}) \text{ sel.} = (F_{\text{out}} \times y_{\text{out}}^i) / (F_{\text{in}} \times y_{\text{in}}^{\text{CO}_2} \times \text{Conv. CO}_2) \times 100\%$$

where F_{in} was the mole flow rate of the feed gas, mol h^{−1}; F_{out} was the mole flow rate of the effluent, mol h^{−1}; and y_{out}^i was the mole fraction of CH₄(CO) in the effluent. Calculation for hydrocarbon product selectivity included gaseous phase and liquid phase products.

Chain growth probability (α) was calculated according to the Anderson–Schulz–Flory model for the product distribution:

$\ln(W_n/n) = n \ln \alpha + \ln[(1 - \alpha)^2/\alpha]$, where n is the number of carbon atoms in a product; W_n is the weight fraction of the corresponding product.

3. Results and discussion

3.1 Phases of the samples

The XRD patterns of the samples are shown in Fig. 1. The characteristic diffraction peaks at 2θ of 24.2° , 33.3° , 35.7° , 40.9° , 49.6° , 54.1° , 62.6° and 64.1° were ascribed to the α -Fe₂O₃ phase²⁹ and those at 2θ of 30.7° , 51.2° and 60.8° were attributed to the tetragonal ZrO₂ phase.³⁰

For samples (a)–(e) before reduction and reaction, as the Zr content increased, the peak strength of α -Fe₂O₃ was gradually diminished, whereas that of ZrO₂ increased. K impregnation did not obviously affect the phases, as shown in samples (b) and (c). The diffraction peaks of α -Fe₂O₃ by the MAHP method were stronger than that obtained by co-precipitation, as shown in samples (b) and (d). For samples (f)–(h) after reaction, the Fe₃O₄ phase was observed *via* the diffraction peaks at 2θ of 18.34° , 30.18° , 36.56° , 43.24° , 53.54° , 57.10° and 62.74° , whereas the α -Fe₂O₃ phase disappeared, suggesting that the iron species are transformed to Fe₃O₄.^{23,31} In contrast, the ZrO₂ phase did not change distinctly before and after the reaction.

The average crystal particle sizes of the α -Fe₂O₃ phase in the samples are shown in Table 1. As the Zr content increased, the particle size of the α -Fe₂O₃ crystal phase, corresponding to the (104) crystal face, increased first and then decreased. With the MAHP preparation method, the crystal particle size of the α -Fe₂O₃ phase in the 5Fe–1Zr sample was 28.1 nm, which was

not a significant change compared with 24.0 nm of 5Fe–1Zr[C] by co-precipitation.

3.2 Textural properties of the samples

To check the effect of the MAHP method on preparation, the SEM images of fresh samples prepared by the MAHP method before K impregnation were taken, as shown in Fig. 2. Samples (a)–(c) were made up of small and uniformly shaped particles with a microscopic morphology; particle size was in the range of 50–60 nm. In contrast, sample (d) prepared by co-precipitation showed large and irregular particles. During MAHP, the OH[−] ions required for precipitation were gradually released by the hydrolysis of urea, and the pH value remained consistent. Moreover, when the hydrothermal temperature reached 170–180 °C, the nucleation might occur faster than the crystal particle growth. These two conditions cause the formation of small and uniform particles.³²

The N₂ adsorption–desorption isotherms of fresh samples before K impregnation are shown in Fig. 3. Samples (a)–(e) prepared by the MAHP method showed the type IV isotherm pattern with H₃-type hysteresis loop, indicating the presence of mesopores in the samples.²¹

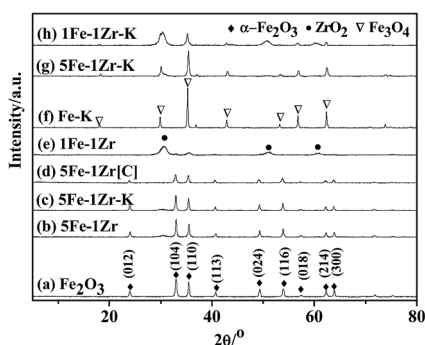


Fig. 1 XRD patterns of the samples. (a)–(e) Before reduction and reaction; (f)–(h) after reaction.

Table 1 Crystal particles of the α -Fe₂O₃ phase

Sample	Size/nm
Fe ₂ O ₃	24.9
7Fe–1Zr	32.7
5Fe–1Zr	28.1
3Fe–1Zr	24.0
1Fe–1Zr	11.1
5Fe–1Zr[C]	24.0

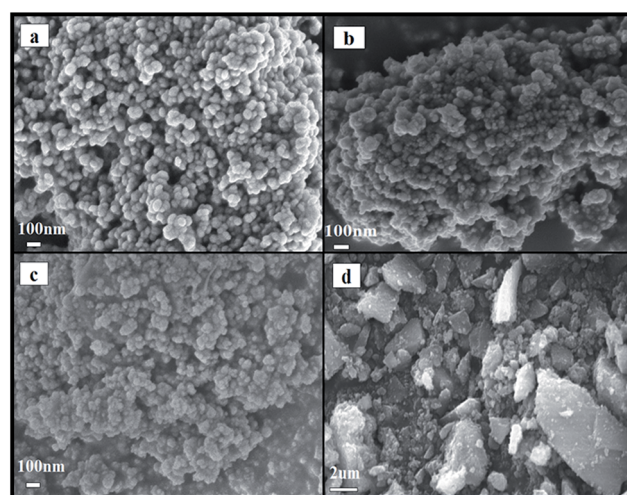


Fig. 2 SEM images of the samples. (a) Fe₂O₃ (b) 7Fe–1Zr (c) 5Fe–1Zr (d) 5Fe–1Zr[C].

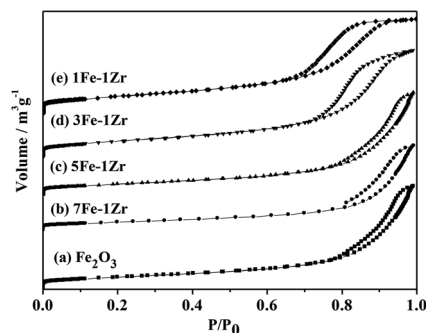


Fig. 3 N₂ adsorption–desorption isotherms of the samples.

Table 2 Pore parameters of the samples

Samples	Surface area (m ² g ⁻¹)	Mesopore volume (cm ³ g ⁻¹)	Micropore volume (cm ³ g ⁻¹)	Mesopore diameter (nm)
Fe ₂ O ₃	22.1	0.092	0.008	2.54
7Fe-1Zr	39.7	0.156	0.014	2.31
5Fe-1Zr	52.6	0.190	0.020	2.25
3Fe-1Zr	76.7	0.191	0.029	11.58
1Fe-1Zr	83.5	0.168	0.032	11.94
5Fe-1Zr[C]	95.3	0.153	0.037	7.32

The pore parameters of fresh samples before reduction and reaction are summarized in Table 2. As the Zr content increased, the surface area and the micropore volume increased. The mesopore volumes of all samples were much larger than the micropore volumes, and 5Fe-1Zr and 3Fe-1Zr showed the maximal mesopore volume. Moreover, 5Fe-1Zr had the minimal mesopore diameter, whereas 1Fe-1Zr had the maximal mesopore diameter. In contrast, 5Fe-1Zr[C] prepared by co-precipitation had the largest surface area, micropore volume, mesopore volume and mesopore diameter.

3.3 Reduction behavior of the samples

From the H₂-TPR profiles of the samples in Fig. 4, it can be seen that all the fresh samples produced two reduction peaks.

For Fe₂O₃ (a), the sharp peak at 280–420 °C and the broad one at 450–800 °C were assigned to the initial reduction of α -Fe₂O₃ to Fe₃O₄, and then the reduction of Fe₃O₄ to α -Fe.³¹ For Fe-K (b), two peaks appeared at low temperatures and were ascribed to the reduction of α -Fe₂O₃ to Fe₃O₄, and the partial reduction of Fe₃O₄ to FeO.¹³ For K-containing samples (b)–(g), the first peaks shifted to high temperatures, suggesting that K modification causes the reduction to be more difficult. The use of a K promoter has also been proved to suppress the adsorption of H₂ to a certain extent.^{12,23} Moreover, the second peaks of 7Fe-1Zr-K (c) and 5Fe-1Zr-K (d) shifted to high temperatures, indicating the inhibition effect on the reduction of Fe₂O₃ and the formation of the iron phase through the FeO phase. With increasing the Zr content in samples (f) and (g), the second peak shifted to lower temperatures, which is coincident with the reported results that Zr addition improves the dispersion of iron phases and makes iron species easily reduced.³³ These results

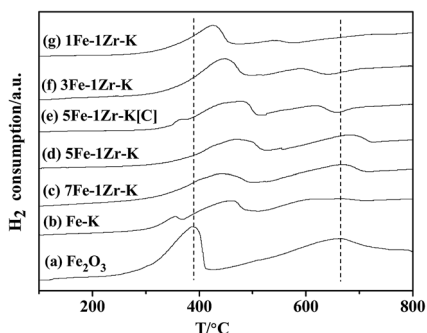
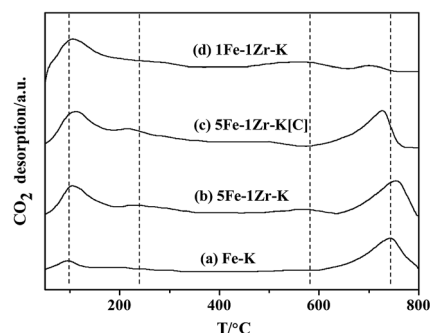
demonstrate that there exists an interaction between the iron species and zirconia, and it was the strongest in 5Fe-1Zr-K. The reducibility of sample 5Fe-1Zr-K[C] by co-precipitation was different from that by the MAHP method. Similar to Fe-K (b), two reduction peaks appeared at low temperatures for 5Fe-1Zr-K[C] (e). The second peak was at 500–650 °C, lower than that of the corresponding 5Fe-1Zr-K, implied that the reduction of Fe₃O₄ to α -Fe is relatively easy.

3.4 Surface adsorption behavior of the samples

Fig. 5 shows the CO₂-TPD profiles of fresh samples after the H₂ pretreatment but before the reaction. Sample Fe-K (a) displayed two CO₂ desorption peaks at 120–170 °C and 610–800 °C. After the addition of Zr, the peak slightly shifted to high temperatures and the CO₂ desorption amount increased, as shown for sample (b). In addition, two new desorption peaks appeared at 200–320 °C and 510–620 °C. The data suggest that the adsorption of CO₂, which is related to surface basicity,¹² is intensified due to the ZrO₂ formation by Zr addition. With further addition of Zr in sample (d), the high temperature desorption peak dramatically decreased. By comparison, the high temperature desorption peak strength of 5Fe-1Zr-K[C] (c) was weaker since the desorption peak temperature was lower.

3.5 Surface composition of the samples

The XPS spectra of fresh samples before reduction and reaction are shown in Fig. 6. For all samples in Fig. 6-A, the binding energies (BE) at 710.9 eV and 724.5 eV were ascribed to Fe(2p_{3/2}) and Fe(2p_{1/2}), respectively. The satellite peak at 718.9 eV characterized the existence of Fe₂O₃.²¹ In Fig. 6-B, the BE at 182.1 eV was attributed to Zr(3d_{5/2}) of ZrO₂. K addition in Fig. 6-A(b)

Fig. 4 H₂-TPR profiles of the samples.Fig. 5 CO₂-TPD profiles of the samples.

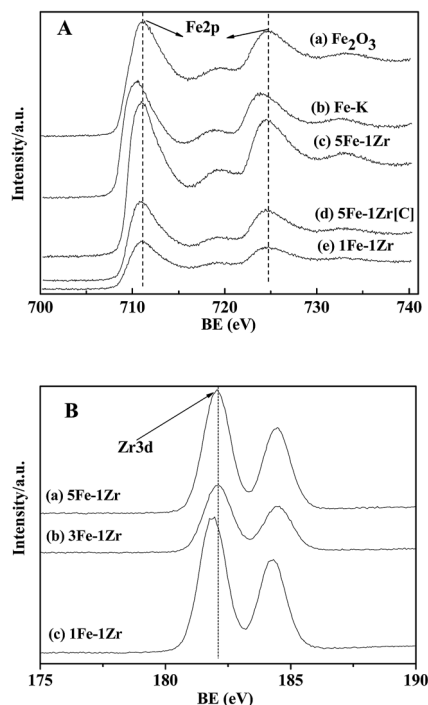


Fig. 6 XPS spectra of the samples.

caused a slight decrease in the BE of $\text{Fe}(2p_{1/2})$ compared with Fe_2O_3 (a). It was proposed that K lowers the metal work function by donating electrons to the vacant d orbits of the iron, enhancing the dissociative adsorption of CO , whereas lowering the H_2 adsorption ability.³⁴ Furthermore, the BE of $\text{Fe}(2p_{3/2})$ and $\text{Zr}(3d_{5/2})$ were lowered for the Fe–Zr samples in Fig. 6-A(c)–(e) and in Fig. 6-B(a)–(c), indicating the increased interaction between the iron species and zirconia.

It can be seen from Fig. 7 that after the reaction, the BE of $\text{Fe}(2p_{3/2})$ in 5Fe–1Zr–K shifted slightly towards low energy, compared with those before reduction and reaction, suggesting the existence of Fe_3O_4 in accordance with the XRD results. The binding energy of the carbon species in the 5Fe–1Zr–K sample is shown in Fig. 8. Before and after reaction, there was carbon (C1s, BE: 284.8 eV) on the sample surface, whereas carbidic carbon (BE: 283.1–283.4 eV)²¹ was not observed. This suggests that the carburization of Fe probably occurs during the reaction, and after reaction the Fe species transform to iron oxides.

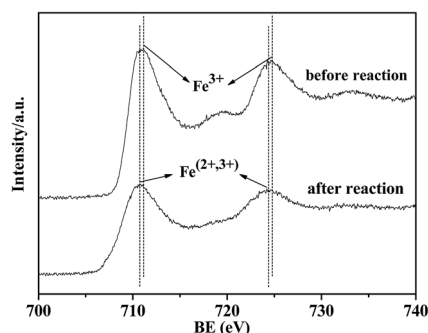


Fig. 7 $\text{Fe}(2p)$ binding energy in 5Fe–1Zr–K.

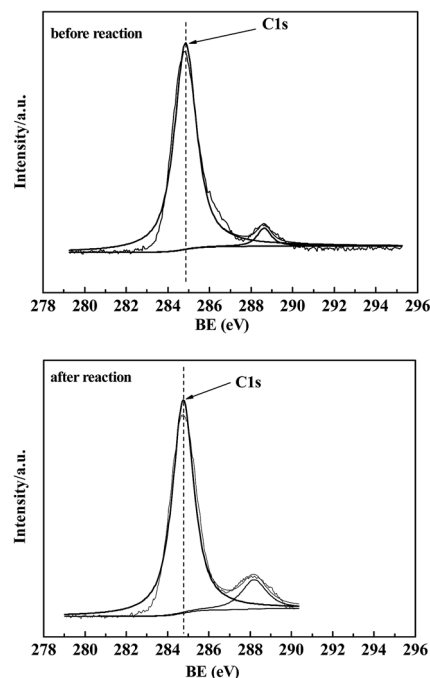


Fig. 8 C(1 s) binding energy in 5Fe–1Zr–K.

From the atomic concentration of the XPS spectra, the atomic Zr/Fe ratios of the samples were calculated. As shown in Fig. 9, the calculated Zr/Fe ratios are higher than the preparation ratios, revealing that Zr is enriched on the sample surface and the enrichment is stronger on 5Fe–1Zr[C] than on 5Fe–1Zr.

3.6 Catalytic activity for CO_2 hydrogenation

The catalytic activities of the samples for CO_2 hydrogenation under selected conditions are shown in Table 3. It can be seen that all samples prepared by the MAHP method showed higher activity with CO_2 conversion above 43%. The main products were hydrocarbons, except for CO and small amounts of oxygenates. The 5Fe–1Zr–K sample displayed the maximum CO_2 conversion of 54.36%. In addition to presenting uniform particles with better dispersion, 5Fe–1Zr–K had the strongest surface basicity as the CO_2 -TPD profile shows in Fig. 5, which should be favorable for the CO_2 adsorptive activation and conversion.

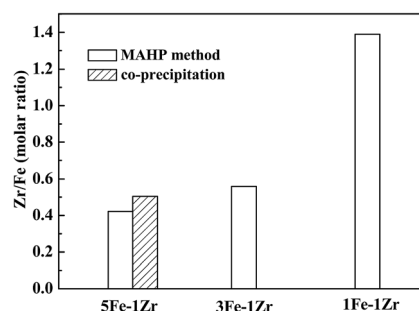


Fig. 9 Atomic Fe/Zr molar ratios on the sample surface.

Table 3 Catalytic activity of the samples for CO₂ hydrogenation^a

Catalysts	CO ₂ Conv./%	Sel./%			Hydrocarbon distribution ^d /C%				O/P
		CO	HC ^b	Oxy. ^c	CH ₄	C ₂ ⁼ –C ₄ ⁼	C ₂ ⁰ –C ₄ ⁰	C ₅ ⁺	
Fe–K	48.33	7.45	89.17	3.38	16.12	50.53	6.69	26.67	7.55
7Fe–1Zr–K	49.78	7.10	91.84	1.06	19.62	52.70	8.45	19.21	6.24
5Fe–1Zr–K	54.36	3.00	96.58	0.42	19.78	53.63	8.33	18.26	6.44
3Fe–1Zr–K	51.55	6.16	90.39	3.45	21.77	50.61	9.94	17.68	5.09
1Fe–1Zr–K	43.43	9.88	90.11	0.01	24.74	46.61	14.20	14.46	3.28
5Fe–1Zr–K[C]	34.02	4.47	94.61	0.92	19.74	48.82	7.92	23.51	6.17

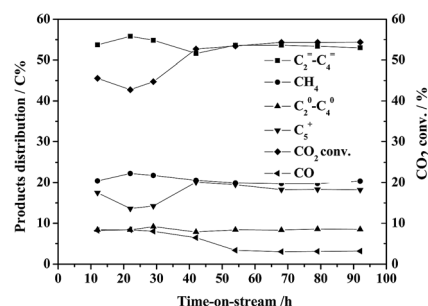
^a Reaction conditions: H₂/CO₂ = 3/1, GHSV = 1000 h^{–1}, 2 MPa, 320 °C. ^b HC: hydrocarbons. ^c Oxy.: oxygenates. ^d C₂⁼–C₄⁼: C₂–C₄ olefins; C₂⁰–C₄⁰: C₂–C₄ paraffins; C₅⁺: C₅⁺ hydrocarbons.

In the production distribution, the CH₄ selectivity over Fe–K was lower than that over Fe–Zr–K but the CO and C₅⁺ selectivity were high. As the Zr content increased, the CH₄ selectivity was gradually increased, whereas the C₅⁺ selectivity decreased, indicating that the Zr addition in the catalyst samples suppresses the formation of the C₅⁺ (heavy) products. As the Fe/Zr ratio increased, the CO₂ conversion and the selectivity of light olefins (C₂⁼–C₄⁼) first increased and then decreased. At the Fe/Zr ratio of 5, the CO₂ conversion and the C₂⁼–C₄⁼ selectivity reached the maxima of 54.36% and 53.63%, respectively, while the selectivity of CO was the lowest (3%). The O/P ratio in the C₂–C₄ hydrocarbon products was 6.44. Considering the interaction between iron species and zirconia indicated by the aforementioned XPS results (Fig. 6) as well as the H₂-TPR results (Fig. 4), it is likely that during the reduction of the samples zirconia would also lower the metal work function by donating electrons to iron and enhance the adsorption of CO while reducing the H₂ adsorption, resulting in an increase in the light olefin products.

In contrast, the 5Fe–1Zr–K[C] catalyst prepared by co-precipitation showed the lowest CO₂ conversion, although better product distribution. As shown in Fig. 9, Zr tends to have more enrichment on the catalyst surface prepared by co-precipitation. This enrichment might reduce the active site number on the catalyst surface, influencing the Fe–Zr interaction and the catalytic activity. Furthermore, the weaker surface basicity of 5Fe–1Zr–K[C] than that of 5Fe–1Zr–K (see Fig. 5) is unfavorable for the CO₂ adsorptive activation.

It has been reported that the steady state establishment of F–T synthesis over iron catalysts can be divided into five episodes of distinct kinetic regimes, which last for about 60 h. As the reaction time is extended, Fe species undergo transformation from iron oxide to iron carbide (Fe₅C₂).³⁵

Fig. 10 shows the catalytic activity of CO₂ hydrogenation over 5Fe–1Zr–K and the production changes at set reaction conditions with time-on-stream. It is clear that the catalytic activity exhibited an induction period of about 60 h. At the initial reaction stage, the CO₂ conversion increased as the active phase iron carbide was gradually formed. After 60 h, both the CO₂ conversion and the C₂⁼–C₄⁼ selectivity remained above 55% and 53%, respectively. The CO selectivity was retained at 3% from the incipient about 8%. The preceding characterization

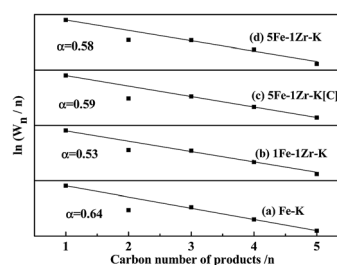
Fig. 10 CO₂ hydrogenation over 5Fe–1Zr–1K with time-on-stream.

indicates that there exists an interaction between iron species and zirconia, which might play a stable role in the active phase of the catalysts.²⁶

Chain growth probability (α) for CO₂ hydrogenation over the catalyst samples is shown in Fig. 11. With Zr addition, α tends to decrease. As the Zr content increases, α decreases from 0.64 over Fe–K to 0.53 over 1Fe–1Zr–K. This is well in accordance with the hydrocarbon product distribution in Table 3, *i.e.*, CH₄ increases, while C₅⁺ hydrocarbons decrease. The α over 5Fe–1Zr–K[C] is higher than that over 5Fe–1Zr–K, and there is more formation of C₅⁺. Moreover, the $\ln(W_n/n)$ values for C₂ hydrocarbons show negative deviation to the fitted line. As the α decreases, the deviation tends to diminish, implying that the secondary reactions of C₂ towards heavy products are likely suppressed.

These results demonstrate that on the one hand, addition of certain amounts of Zr to Fe–K by the MAHP method can

Reaction conditions: H₂/CO₂ = 3/1, GHSV = 1000 h^{–1}, 2 MPa, 320 °C

Fig. 11 α value of CO₂ hydrogenation over the catalyst samples.

improve the dispersion of active Fe on the uniform catalyst particles during the course of reduction/reaction and promote the uptake and activation of CO₂ by increasing the surface basicity on the catalyst surface. On the other hand, the Fe–Zr interaction shows a positive effect toward stabilizing the catalysts. The CO₂ hydrogenation activity towards light olefins is thus improved.

4. Conclusion

The precursors of Fe–Zr–K catalysts prepared by the microwave-assisted homogeneous precipitation method produced small and uniform particles and improved the dispersion of iron species. After reduction, they showed high activity for the hydrogenation of CO₂ to light olefins. Addition of appropriate amounts of Zr promoter, and K modification can increase the catalyst surface basicity and the interaction between iron species and zirconia, resulting in significant improvement in the CO₂ conversion and the product distribution. When the Fe/Zr ratio was 5, the CO₂ conversion and the light olefins selectivity reached the maxima with the highest O/P ratio in the C₂–C₄ hydrocarbon product fraction. Moreover, the selectivity of CO was reduced as low as 3%. After the induction period, the catalyst remained stable up to 92 h in time-on-stream reaction.

Acknowledgements

Financial supports from the Special Prophase Project on Basic Research of Department of Science and Technology of China (Grant No. 2012CB723106) and the Natural Science Foundation of China (Grant No. 21366025) are greatly acknowledged.

References

- 1 M. Mikkelsen, M. Jørgensen and F. C. Krebs, *Energy Environ. Sci.*, 2010, **3**, 43–81.
- 2 R. W. Dorner, D. R. Hardy, F. W. Williams and H. D. Willauer, *Energy Environ. Sci.*, 2010, **3**, 884–890.
- 3 W. Wang, S. Wang, X. Ma and J. Gong, *Chem. Soc. Rev.*, 2011, **40**, 3703–3727.
- 4 M. He, Y. Sun and B. Han, *Angew. Chem., Int. Ed.*, 2013, **52**, 2–16.
- 5 G. Centi, E. A. Quadrelli and S. Perathoner, *Energy Environ. Sci.*, 2013, **6**, 1–19.
- 6 S. Zhang, H. Yan, M. Wei, D. G. Evans and X. Duan, *RSC Adv.*, 2014, **4**, 30241–30249.
- 7 G. D. Weatherbee and C. H. Bartholomew, *J. Catal.*, 1984, **87**, 352–362.
- 8 T. Riedel, G. Schaub, K. Jun and K. Lee, *Ind. Eng. Chem. Res.*, 2001, **40**, 1355–1363.
- 9 M. Lee, J. Lee and C. Chang, *Bull. Chem. Soc. Jpn.*, 1989, **62**, 2756–2758.
- 10 M. Lee, J. Lee and C. Chang, *J. Chem. Eng. Jpn.*, 1990, **23**, 130–136.
- 11 J. Lee, W. Chern and M. Lee, *Can. J. Chem. Eng.*, 1992, **70**, 511–515.
- 12 P. H. Choi, K. Jun, S. Lee, M. J. Choi and K. W. Lee, *Catal. Lett.*, 1996, **40**, 115–118.
- 13 G. Kishan, M. Lee, S. Nam, M. Choi and K. Lee, *Catal. Lett.*, 1998, **56**, 215–219.
- 14 T. Herranz, S. Rojas, F. J. Pérez-Alonso and J. L. G. Fierro, *Appl. Catal., A*, 2006, **311**, 66–75.
- 15 J. Kim, S. Lee, S. Lee, M. Choi and K. Lee, *Catal. Today*, 2006, **115**, 228–234.
- 16 P. S. Sai Prasad, J. W. Bae, K. Jun and K. W. Lee, *Catal. Surv. Asia*, 2008, **12**, 170–183.
- 17 R. W. Dorner, D. R. Hardy, F. W. Williams and H. D. Willauer, *Appl. Catal., A*, 2010, **373**, 112–121.
- 18 R. W. Dorner, D. R. Hardy, F. W. Williams and H. D. Willauer, *Catal. Commun.*, 2011, **15**, 88–92.
- 19 Z. You, W. Deng, Q. Zhang and Y. Wang, *Chin. J. Catal.*, 2013, **34**, 956–963.
- 20 M. Martinelli, C. G. Visconti, L. Lietti, P. Forzatti, C. Bassano and P. Deiana, *Catal. Today*, 2014, **228**, 77–88.
- 21 M. Al-Dossary, A. A. Ismail, J. L. G. Fierro, H. Bouzid and S. A. Al-Sayari, *Appl. Catal., B*, 2015, **165**, 651–660.
- 22 G. P. van der Laan and A. A. C. M. Beenackers, *Catal. Rev.: Sci. Eng.*, 1999, **41**, 255–318.
- 23 J. Wang, Z. You, Q. Zhang, W. Deng and Y. Wang, *Catal. Today*, 2013, **215**, 186–193.
- 24 V. R. Rao Pendyala, G. Jacobs, J. C. Mohandas, M. Luo, W. Ma, M. K. Gnanamani and B. H. Davis, *Appl. Catal., A*, 2010, **389**(1–2), 131–139.
- 25 J. O. R. Wambach, A. Baiker and A. Wokaun, *Phys. Chem. Chem. Phys.*, 1999, **1**, 5071–5080.
- 26 A. A. Hakeem, R. S. Vásquez, J. Rajendran, M. Li, R. J. Berger, J. J. Delgado, F. Kapteijn and M. Makkee, *J. Catal.*, 2014, **313**, 34–45.
- 27 F. Bondioli, A. M. Ferrari, C. Leonelli, C. Siligardi and G. C. Pellacani, *J. Am. Ceram. Soc.*, 2001, **84**, 2728–2730.
- 28 J. Du, Y. Zhang, T. Tian, S. C. Yan and H. T. Wang, *Mater. Res. Bull.*, 2009, **44**, 1347–1351.
- 29 Ş. Özkara-Aydinoğlu, Ö. Ataç, Ö. F. Gül, Ş. Kınayyigit, S. Şal, M. Baranak and İ. Boz, *Chem. Eng. J.*, 2012, **181–182**, 581–589.
- 30 V. G. Deshmane and Y. G. Adewuyi, *Microporous Mesoporous Mater.*, 2012, **148**, 88–100.
- 31 W. Ning, N. Koizumi, H. Chang, T. Mochizuki, T. Itoh and M. Yamada, *Appl. Catal., A*, 2006, **312**, 35–44.
- 32 J. Baneshi, M. Haghighi, N. Jodeiri, M. Abdollahifar and H. Ajamein, *Energy Convers. Manage.*, 2014, **87**, 928–937.
- 33 K. Chen, Y. Fan and Q. J. Yan, *Chin. J. Catal.*, 1995, **16**, 433–436.
- 34 M. E. Dry, T. Shingles, L. J. Boshoff and G. J. Oosthuizen, *J. Catal.*, 1969, **15**, 190–199.
- 35 H. Schulz, T. Riedel and G. Schaub, *Top. Catal.*, 2005, **32**, 117–124.